Proton radiography of laser-driven imploding target in cylindrical geometry

L. Volpe,[1] D. Batani,[1,2] B. Vauzour,[3] Ph. Nicolai,[3] J. J. Santos,[3] C. Regan,[3] A. Morace,[4] F. Dorchies,[3] C. Fourment,[3] S. Hulin,[3] F. Perez,[5] S. Baton,[5] K. Lancaster,[6] M. Galimberti,[6] R. Heathcote,[6] M. Tolley,[6] Ch. Spindloe,[6] P. Koester,[2] L. Labate,[2] L. A. Gizzi,[2] C. Benedetti,[7] A. Sgattoni,[7] M. Richetta,[8] J. Pasley,[9] F. Beg,[10] S. Chawla,[10] D. P. Higginson,[10] and A. G. MacPhee[11]

[1]*Università degli Studi di Milano-Bicocca, Piazza della scienza 3, Milano 20126, Italy*
[2]*INO-CNR, Via G. Moruzzi, 1–56124, Pisa, Italy*
[3]*CELIA, Université de Bordeaux, CNRS, CEA, F33405, France*
[4]*Università degli Studi di Milano, Dipartimento di Fisica, via Celoria, 16 1–20133 Milano, Italy*
[5]*LULI, Ecole Polytechnique-CNRS-UPMC, 91128 Palaiseau Cedex, France*
[6]*RAL, STFC, Harwell Science and Innovation Campus Didcot, OX11 0QX, United Kingdom*
[7]*University of Bologna, Via Irnerio 46 Bologna (40126) Italy*
[8]*University of Rome "Tor Vergata," via della Ricerca Scientifica 1, 00133 Roma, Italy*
[9]*Department of Physics, University of York, York, YO10 5DD, United Kingdom*
[10]*University of California San Diego, La Jolla, California 92093, USA*
[11]*LLNL, 7000 East Avenue, Livermore, California 94550, USA*

(Received 19 October 2010; accepted 22 November 2010; published online 24 January 2011)

An experiment was done at the Rutherford Appleton Laboratory (Vulcan laser petawatt laser) to study fast electron propagation in cylindrically compressed targets, a subject of interest for fast ignition. This was performed in the framework of the experimental road map of HiPER (the European high power laser energy research facility project). In the experiment, protons accelerated by a picosecond-laser pulse were used to radiograph a 220 μm diameter cylinder (20 μm wall, filled with low density foam), imploded with ~200 J of green laser light in four symmetrically incident beams of pulse length 1 ns. Point projection proton backlighting was used to get the compression history and the stagnation time. Results are also compared to those from hard x-ray radiography. Detailed comparison with two-dimensional numerical hydrosimulations has been done using a Monte Carlo code adapted to describe multiple scattering and plasma effects. Finally we develop a simple analytical model to estimate the performance of proton radiography for given implosion conditions. © *2011 American Institute of Physics*. [doi:10.1063/1.3530596]

I. INTRODUCTION

Many diagnostics[1] have been used in inertial confinement fusion (ICF) to follow the implosion dynamics, including proton radiography.[2,3] Laser based proton source have also been used in this context, in particular for small-scale experiments performed in the framework of studies on the fast ignition approach to ICF.[4] Here the evolution of targets is imaged using the relatively low-energy (~10 MeV) protons created by the interaction of high intensity (10^{18}–10^{21} W/cm^2) lasers with solid targets.

In this context, we performed an experiment at the Rutherford Appleton Laboratory[5] (RAL) in the framework of the HiPER roadmap[6] with the goal of studying the transport of fast electrons in cylindrically compressed matter.[7–9] Proton radiography was used together with hard x-ray radiography in the first phase of the experiment to record the implosion history of a cylindrical target. Experimental results were compared to simulations performed with the Monte Carlo code MCNPX (Ref. 10) using the two-dimensional (2D) density and temperature profiles of the imploding cylinder obtained with the hydrocode CHIC.[11–13] Laser based protons are characterized by small source, high degree of collimation, and short duration. The multienergetic proton spectrum also allows probing the implosion at different times in a single shot, thanks to the difference in times-of-flight for protons at different energies. This is a clear advantage over other diagnostics (e.g., hard x-ray), which require several shots in order to follow the complete implosion history.

Another advantage of using proton radiography is a simple experimental setup keeping the imploding cylinder between the proton target and the proton detector on the same axis (whereas x-ray radiography needs a complex geometry, crystals, collimators, and detector alignment).

Proton radiography using laser-generated protons, and radiochromic films (RCFs) as detectors, has already been used in an experiment at RAL (Refs. 4 and 5) to probe the implosion of a spherical shell. Experimental results were analyzed and compared with Monte Carlo (MC) simulations in Ref. 4. However, the analysis done in Ref. 4 is based on the usual approach to proton imaging in which the proton energy loss during the target penetration is neglected assuming a direct correspondence between time-of-flight and stopping range of proton inside the detector. This approach has proven to be very successful in the detection of electric and magnetic fields in plasmas,[14,15] but, as we will show in the following, it falls if applied to a the typical ICF. Starting from this point of view, in Ref. 4 the authors associated one RCF layer to a given probing time, and actually restricted most of their analysis to the image of the imploding shell obtained in the layer corresponding to the Bragg peak for 7

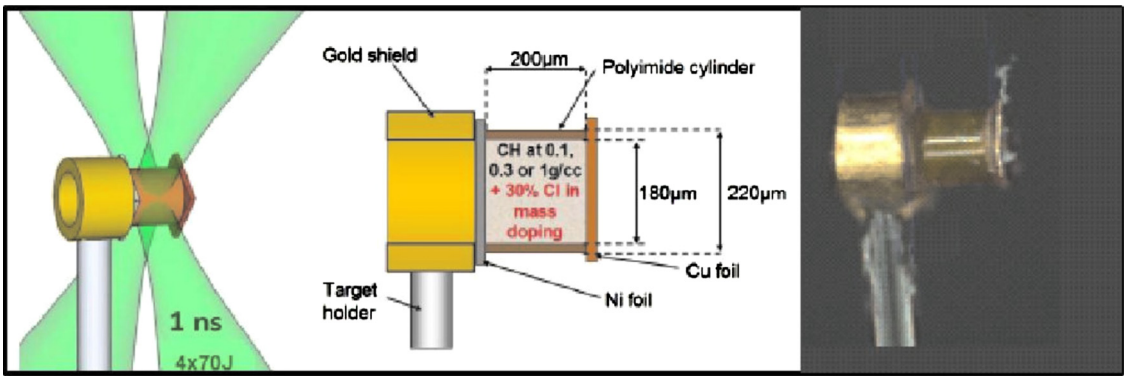

FIG. 1. (Color online) (left) Schematic of the four compression beams (each of 1 ns) focused on the plastic cylinder. (right) Real target: left side is the gold shielding cylinder and right side is the plastic cylinder filled with low density foam.

MeV, protons which they relied to a time of ~2 ns after the beginning of laser irradiation (~1 ns before stagnation). They observed significant differences between size of the shell predicted by the hydrocodes (85 mm) and the size recorder on RCF images (120 mm). They justify this difference on the basis of the scattering of protons in the compressed core (although, according to their estimates, they get 160 μm) and of the presence of electric and magnetic fields affecting proton trajectories.

In reality, as we will show in this paper, the problem mainly lies in the fact that, as protons are penetrating thick and dense targets, they do suffer severe multiple scattering (MS) effects and energy losses. This means that the (spatial) information carried on by the protons traveling in the central high density region of the target is lost and the image on the detector is mainly formed by the protons coming from the lower density regions. These effects have previously been considered in static proton radiography by Roth *et al.*,[16] but acquire a new and deeper meaning in our dynamic situation, bringing to mixing of the images formed by protons with different energies. This implies that a more careful analysis of RCF images is needed, dropping the simple layer-to-time correspondence, and requiring detailed comparison with computer simulations. Whenever such analysis is done (see Sec. IV), we get a good agreement between experimental results and hydrosimulations.

The low density and hot temperature plasma corona play fundamental rules in formation of image on detector due to the relative low proton energy. Here indeed we show that at these conditions the stopping power (ST) in plasma is higher than that in solid target. Finally, from the experimental point of view, in our work we could compare proton radiography results with those obtained by hard x-ray radiography, allowing to better understand the performance as well as the limitations of proton diagnostic, and to validate our interpretation of proton images.

II. EXPERIMENTAL SETUP

The experiment was carried out at the Vulcan facility using four long-pulse laser beams driving the implosion of cylindrical target. The beams ($\sim 4\times 50-4\times 70$ J in 1 ns at $\lambda=0.53$ μm) were focused to 150 μm full width at half maximum (FWHM) spots as shown in Fig. 1. A short pulse (SP) beam (100–150 J in 1 ps) was focused as a backlighter source by an $F=3.5$ off axis parabola with a focal spot 20 μm FWHM at a peak irradiance of 1.5×10^{19} W/cm^2 to produce protons for radiography. An intense beam (10 ps, 160 J) is focused on a 25 μm titanium foil providing the source for hard x-ray radiography at $h\nu\approx 4.5$ keV (details of such diagnostic will be presented in another paper).

The 200 μm long polyimide cylindrical tube (Fig. 1) with 220 μm outer diameter and 20 μm wall thickness was filled with foam (acrylate) at density 0.1 g/cc, 1 g/cc, or empty. One side was closed with a Cu foil, the other side was closed by a Ni foil. The timing of the four long pulse (LP) beams was set so that they hit simultaneously the cylinder with the precision of ± 50 ps due to the jitter. The delay between LP and SP was adjustable from 0 to 3.6 ns. The target was designed in order to generate plasmas with different values of density and temperature and thus different plasma domains.

The experiment was split into two phases. The first phase objective was to determine the hydrodynamic characteristics of the compressed matter, i.e., its temperature and density at optimal compression while the second phase of the experiment was designed to measure the hot electron propagation through the compressed matter. In this paper we report about the first phase; for a complete report of the second phase see Refs. 7–9.

A. X-ray radiography setup

A SP laser beam (10 ps, 160 J at $\lambda=1.064$ μm) was focused on a 25 μm thick Ti foil placed at distance $d=10$ mm transversally of the target. The focal spot was 20 μm diameter and the laser intensity on the foil was 5×10^{18} W/cm^2. The generated x-rays were used to probe the cylinder during the compression. The transmitted x-ray Kα radiation (Ti-Ka ~4.5 keV) was selected via a spherically bent quartz crystal (quartz 203, $2d=2.749$ A, $R_c=380$ mm) at Bragg incidence ($\theta_{\mathrm{Bragg}}\sim 89:5°$) and located at a distance $L_1=210$ mm from the target on the opposite side of the Ti foil. The cylindrical target was imaged on to imaging plate, placed at $L_2\sim 2$ m away from the crystal (see Fig. 2). The total magnification of the imaging

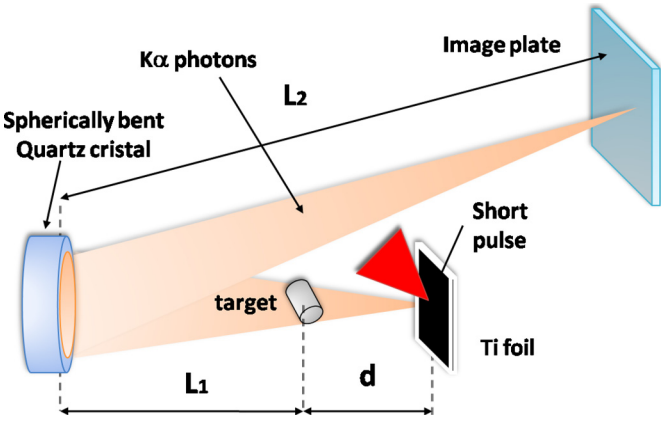

FIG. 2. (Color online) Schematic of the x-ray radiography setup.

system was $M_{XR}=10.8$ and the spatial resolution was $\Delta x \sim 20$ μm. The schematic is shown in Fig. 2.

B. Proton radiography setup

Transverse point projection proton radiography[4,9] was used to measure the target density during the compression. The proton backlighter source was realized using the SP laser beam from the Vulcan laser facility providing 100 J at 1.064 μm in a 1 ps pulse. The laser beam was focused at normal incidence on a 20 μm gold foil located at distance $d=10$ mm on the side of the cylindrical target. The obtained intensity on the gold foil was 3×10^{19} W/cm^2 for a focal spot of 20 μm FWHM. The emitted proton beam from the Au foil's rear side transversally probed the compressed cylinder. Protons had an approximately exponential spectrum with a cut-off energy of $\sim$10 MeV and they were collected by a stack of RCF composed of five layers of HD-810 and ten layers of MD55 positioned at a distance $L\sim35$ mm away from the target. The theoretical magnification of the system is $M_{PR}=1+L/d\sim4.5$. A protective Al foil (12 μm thick) was also positioned in front of the first RCF layer giving minimum detectable proton energy of $\sim$1 MeV the schematic is shown in Fig. 3. The measured optical density on each RCF active layer is proportional to deposited energy.[17]

III. EXPERIMENTAL ANALYSIS

A. X-ray radiography results

Here we show the main results of x-ray radiography and refer for a more detailed analysis in Ref. 8. X-rays are not affected by MS as protons are. The principal limitations of the diagnostic lie in the imaging resolution power. The latter depends on the crystal quality, the x-ray source size, and the detector efficiency. The resolution power of the imaging system has been measured to be $\Delta x=20$ μm by radiographing a metal grid whose dimensions (step size and thickness) are known. On Fig. 4 a typical image of the cylinder is presented, as obtained with the x-ray radiography. X-ray transmission profiles are extracted from radiographies by doing a lineout of the compressed part of the cylinder. Experimental diameters (FWHM) are estimated by fitting the experimental transmission profiles with super-Gaussian of fourth order (for early times, i.e., when the cylinder's boundaries are still sharp) or Gaussian (close to the stagnation time, i.e., when the blurring is more important) functions.

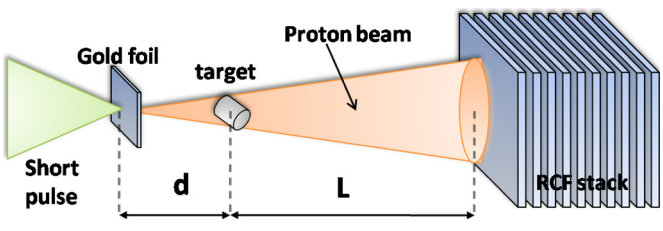

FIG. 3. (Color online) Schematic of the proton radiography setup.

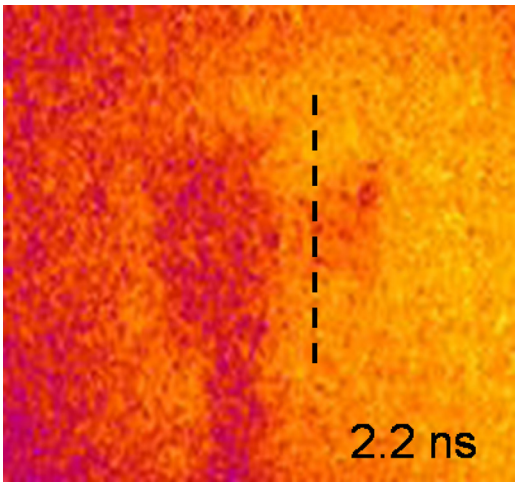

FIG. 4. (Color online) X-ray radiography of the same target during compression (at $t=2.2$ ns). The white dashed line which corresponds to the maximum compression refers to the position of the line out used to estimate the FWHM of the cylinder core along the line.

B. Proton radiography results

The images recorded on RCFs were digitized with a Nikon 4.0 scanner with 4000 dots per inch resolution ($\sim$6.5 μm). In our experimental setup (see Fig. 2) the geometrical magnification was $M=4.5$ allowing a spatial resolution of $\sim$1.5 μm. We typically got seven impressed RCF layers per shot covering a full time span of 500 ps. Therefore we could not follow the whole target implosion in one shot, which implied the need to change the delay between SP and LP and reconstruct the full implosion with different shots (typically three). The difference in Bragg peak energy between two successive layers corresponded to a mean time-of-flight difference of $\sim$60 ps.

An example of experimental radiographs of the cylinder before compression (reference shot) and of different stages of compressions is shown below in Fig. 5.

It is clear that compression along the longitudinal direction (cylinder axis) is not uniform. This is due to the finite size of the LP focal spots (comparable to the cylinder length). However the focal spot was large enough to allow neglecting three-dimensional effects around its center. Therefore for each RCF image, we draw the optical density profile

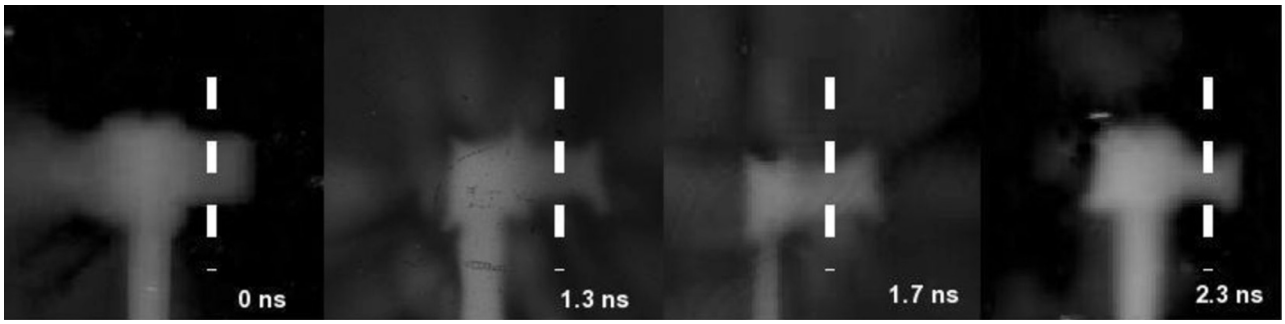

FIG. 5. Compression history obtained by experimental proton radiographs at $t_1=0$ ns, $t_2=1.3$ ns, $t_3=1.7$ ns, and $t_4=2.3$ ns.

at maximum compression (as shown later in Fig. 8) and measured its FWHM. The optical density profile could be well interpolated by a super-Gaussian at early times (including the initially cold cylinder) while approaching the stagnation time the fit becomes more Gaussian. This reflects the transition from a sharp cylinder boundary at early times to an extended plasma corona later. The measured widths were compared to the diameter of the compressed cylinder obtained by hydrosimulations, which assumed no variation of the intensity along the longitudinal direction. Let us also notice that compression was not uniform in the polar direction too, as a consequence of the small number of LP beams (only four). This implies a different target compression at 0° (direction of one of the incident LP beams) and at 45° (direction exactly between two LP beams), an effect which was taken into account by 2D simulations. Therefore the viewing angle of the proton diagnostic also needed to be considered when comparing experimental results to hydro simulations using CHIC code.

The CHIC code includes bidimensional axisymmetrical hydrodynamics based on a cell-centered Lagrangian scheme, electron and ion conduction, thermal coupling, and detailed radiation transport. In our case, the ionization and opacity data are tabulated assuming a local thermodynamic equilibrium, depending on the plasma parameters. The equations of state implemented in the code are based on a QEOS model[13] or SESAME tables.[14] Density (Fig. 6), temperature [Fig. 7 (left)], and ionization degree [Fig. 7 (right)] profiles at different time during target compression, obtained by running CHIC, are shown below.

Figure 8 shows the time evolution of the cylinder diameter compared to the numerical prediction from the hydrosimulations in Figs. 6 and 7 for the case of a cylinder filled with 0.1 g/cc foam. It clearly shows the trend of compression of the target and it also reproduces the stagnation time given by simulations quite well (~2.1 ns). Note that the estimation of the stagnation time was obtained starting from different hydroprofiles obtained by CHIC code relative to different laser energies in MC simulations (stagnation time is a strong function of driver energy) and choosing the best fit with experimental data (the right parameters are those used in Fig. 6). It is clear however that the absolute value of the diameter of the compressed cylinder is not reproduced. In particular, the minimum observed diameter is ~140 μm against ~50 μm given by hydrosimulations (see Fig. 6) for the same stagnation time. Moreover the x-ray radiography results confirm the hydrosimulations prediction giving a minimum observed diameter of ~80 μm. This fact implies that low energy protons are not able to probe the dense core as deeply as x-rays do.

IV. MC SIMULATION

In order to investigate the physical reason of the apparent contradiction among protons, x-ray results, and hydroexpectation value showed in Fig. 8, we have run MC simulations using the code MCNPX developed at LANL.[10] MCNPX is a general-purpose MC N-particle code that can be used for neutron, photon, electron, protons, and other particles transport. The MC code is able to reproduce the experimental setup in all its relevant parts: the proton source (energy spectrum and spatial distribution of the proton source obtained from RCF analysis), the target and detector characteristic (material composition, density profile, and geometry). ST of protons in the target is described by using Bethe's theory[18] while MS effects are described by Rossi's theory.[19]

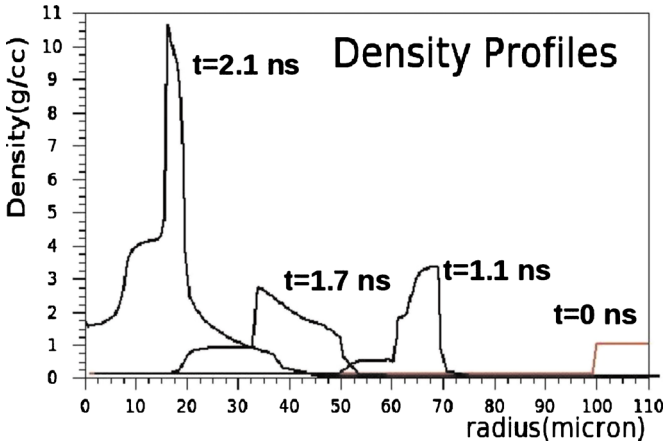

FIG. 6. (Color online) Radial density profiles of cylindrical target before compression ($t=0$ ns) and during the compression phase ($t=1.1, 1, 7, 2.1$ ns). The simulations are performed with CHIC code using ~150 J of laser light at $\lambda=0.53$ mm in four symmetrically laser beams on a 200 mm long polyimide cylindrical tube with 220 mm outer diameter and 20 mm wall thickness filled with a plastic foam of density 0.1 g/cc.

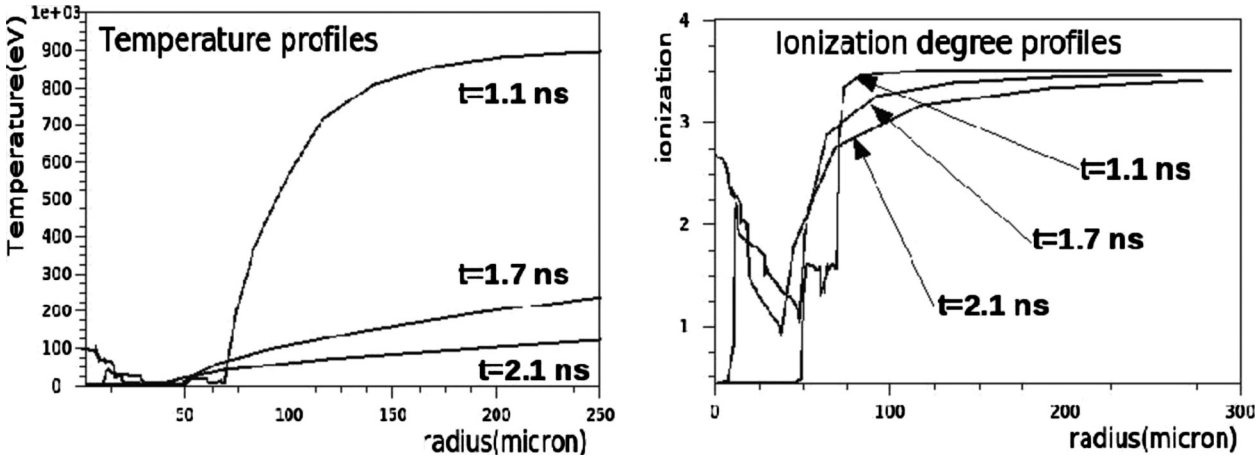

FIG. 7. Radial temperature (left) and ionization degree (right) profiles of cylindrical target during the compression phase ($t=1.1,1,7,2.1$ ns). The simulations are performed with CHIC code in the same conditions of Fig. 6. Note that the ionization value 3.5 corresponds to the "mean" maximum ionization for the chemical composition of the compressed target.

A. Plasma effects

Here we introduced some modifications in order to account for the differences between Bethe's theory and the actual ST in plasmas. Such "plasma effects," connected to the variation of parameters (density, temperature, and ionization degree in Figs. 6 and 7) during target implosion, must be taken into account comparing MC simulations with experimental data and hydrodynamic simulations. Indeed in our experiment, there is a significant region (plasma corona) in which the temperature becomes very high [$T\sim 1$ keV see Fig. 7 (left)] which implies a large number of free electrons (ionization degree) with respect to the bound electrons and a correspondent enhancement of SP. Conventional MC codes such as MCNPX, FLUKA, and SRIM do not take into account such effects because they were built to describe particle transport in cold matter (i.e., temperature and ionization effects are not taken into account).

A number of theoretical studies on ion beam interaction with plasmas are found in literature[20,21] and an experimental proof of the increase of the ion ST in ionized target material has been obtained in Ref. 22. A self-consistent theory of energy loss of ions in plasmas is given by means of the Vlasov–Poisson equations.[21] Our analysis is developed within this framework and leads to the following formula for ST in partially ionized plasma (all the details are shown in the Appendix):

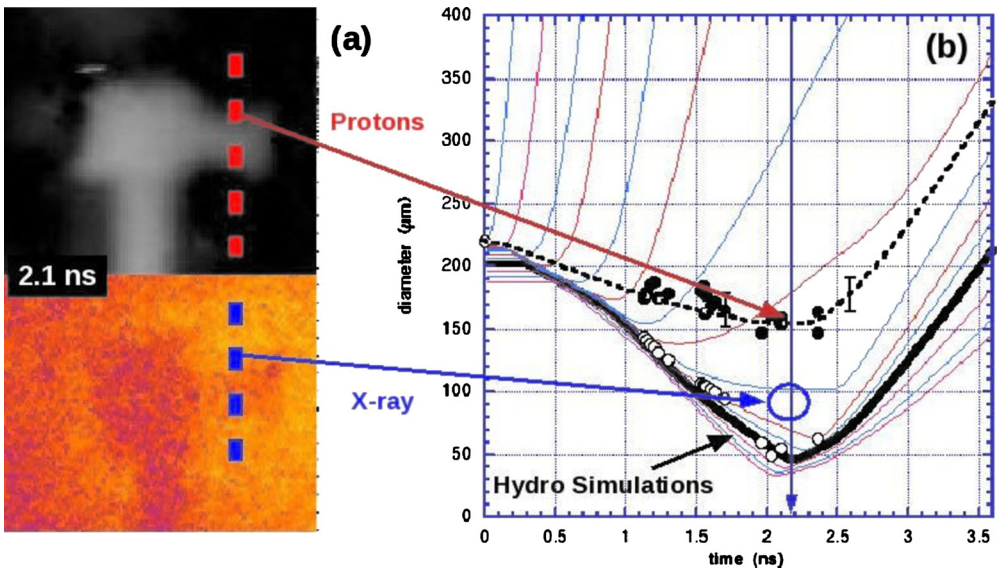

FIG. 8. (Color online) (a) Comparison of hard x-ray radiography (below) and proton radiography (above) obtained around the stagnation time (~2.1 ns), showing how hard x-rays probe the target to larger densities. In both cases, diameters are measured from FWHM of optical density profiles drawn along the vertical dashed line (corresponding to the waist of the images, i.e., maximum compression). (b) FWHM of the cylinder 1D profiles as a function of time. Experimental (full circle) vs hydrodynamic simulations (empty circle). Continuous lines represent the hydro-dynamic evolution of each point of the cylinder obtained running CHIC code. The stagnation time is the same as predicted in hydrodynamic simulations but proton images show a larger size.

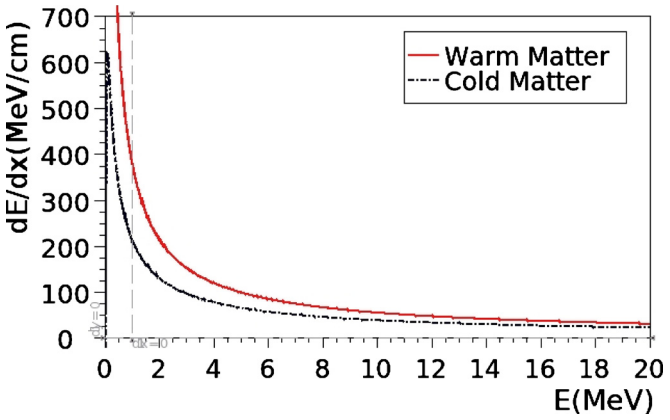

FIG. 9. (Color online) Proton stopping power as a function of energy for cold (line below) and warm matter (line above).

$$\left(\frac{dE}{dx}\right) = 1.23 \times 10^{-9} \frac{\rho}{AE_p}[q_i L_f + (Z - q_i)L_b], \tag{1}$$

where L_f and L_b are, respectively, the free and bound electrons terms [Eqs. (A2) and (A5)]. Equation (1) represent the energy loss by protons with energy E_p(MeV) passing through partially ionized plasma with atomic and mass numbers Z and A, density ρ(g/cc), and ionization degree q_i. The temperature effects are taken into account by the term L_f which is a function of k_bT(eV).

The general equation in Eq. (1) leads to the Bethe ST formula[18] when q_i becomes

$$\left(\frac{dE}{dx}\right)_c = 1.23 \times 10^{-9} \frac{Z\rho}{AE_p} \ln\left(2149 \frac{E_p}{\bar{I}}\right) \tag{2}$$

and lead to the Bohr ST formula[23] when q_i becomes equal to Z

$$\left(\frac{dE}{dx}\right)_p = 1.23 \times 10^{-9} \frac{q_i\rho}{AE_p} \ln\left(235.8 \sqrt{\frac{AE_P^3}{q_i\rho}}\right). \tag{3}$$

Comparison between Bethe and Bohr formula is shown in Fig. 9 as a function of proton energy for the same material (Mylar), temperature $T=1$ keV, and density $\rho=0.1$ g/cc.

This difference showed in Fig. 9 is principally due to the fact that free electrons are excited more easily than bound ones and it seems that it occurs predominantly for low density regions (e.g., $\rho<1$ g/cc). It is important to note that Eqs. (1)–(3) are valid only in the classical free gas approximation [Eq. (A10) in the Appendix], i.e., for low density and high temperature as showed in Fig. 18. One simple way to include plasma effects without changing the code in MCNPX is to replace the "real" density profile (Fig. 6) ρ_h given by hydrosimulation with an "effective" profile ρ_e calculated by imposing the ST used by MC code [Eq. (2)] to be the same as the one which takes place in plasma [Eq. (3)] in the region where the classical free gas approximations are satisfied,

$$\left(\frac{dE}{dx}\right)_c (\rho_e) = \left(\frac{dE}{dx}\right)_p (\rho_h). \tag{4}$$

The effective density depends on the hydrodensity through a factor η which depends on the density, temperature, and ionization degree of the plasma and on proton energy E_p,

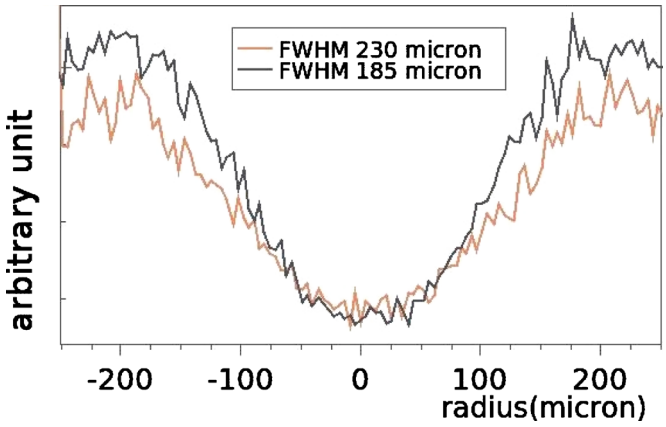

FIG. 10. (Color online) MC simulation of proton energy deposition in layer corresponding to a Bragg peak for $E_p=3.2$ MeV unperturbed protons (MC simulation without cylinder between proton source and detector), taken from the original hydro density profile [above black (dark line)] or using an effective density profile (plasma effects accounted for) [below red (lighter) line

$$\rho_e = \eta\rho_h; \eta = \frac{q_i}{Z}\left(\frac{L_f}{L_b} + \frac{Z - q_i}{q_i}\right). \tag{5}$$

Note that in the low density plasma corona region (fully ionized plasma $q_i=Z$) Eq. (5) becomes $\eta \sim L_f/L_b$ which implies that if $L_f > L_b$ then $\eta > 1$ and $\rho_e > \rho_h$ according to Fig. 9 and with experimental results obtained in Ref. 23. On the other hand, in the solid target region ($q_i=0$) Eq. (5) becomes $\eta=1$ which implies $\rho_e=\rho_h$.

The above mentioned method affect also the estimation of the MS by the MC code introducing a magnification factor in the Rossi formula implemented in the code (the Rossi formula was obtained in plasma configuration). We calculated the error due to the magnification factor which is almost everywhere less than 10% of the ST coefficient. In Fig. 10 are shown two different profiles obtained running MC simulation once with original density profile (ρ_h) and the other with the modified one (ρ_e).

B. Proton energy spectrum

One of the most important ingredients for the MC simulations input file is the spatial and energy distribution of the initial proton beam. This essential information can be obtained by measuring the energy deposited in each RCF layer for a shot in which the cylindrical targets is removed (i.e., protons traveling undisturbed) (Fig. 11). We had uncertainties deriving from shot-to-shot variations in energy and angular distribution of emitted protons.

In particular, following Ref. 24, the energy deposited in the kth RCF layers [Eq. (6)] is given by the convolution of the energy deposition curve $B(z_k,x,y,E)$ (characterized by the presence of the Bragg peak) and the proton energy distribution $P(E,x,y)$,

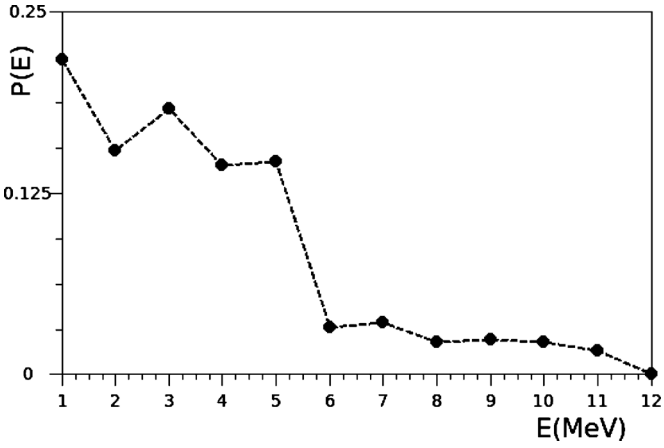

FIG. 11. Spatial integrated initial spectrum $P(E)$ calculated inverting the matrix system obtained by the approximation of Eq. (6) for the case of shot without cylinder.

$$S_k(x,y) = \int_0^{E_{\max}} B_{\Delta z_k}(x,y,E_p) P(x,y,E_p) dE; \tag{6}$$

$$B_{\Delta z_k} = \int_{\Delta z_k} B(z,x,y,E_p) dz.$$

Assuming a discrete energy spectrum according to energy discretization emerging from RCF configuration (the finite number of RCFs layers gives us information about finite value of energy only) we can approximate the integral in Eq. (6) obtaining a matrix system which can be inverted in order to determine the spatial and energy spectrum of the initial proton beam.

In Fig. 9 is shown the spatial integrated initial spectrum function $P(E_i)$ as was obtained solving Eq. (6) for different energies which are related to different RCF layers compared with the corresponding images for a shot without target "free shot." The "almost"'-exponential form (trapezoidal) of the spectral function agrees with typical spectral function form obtained in proton acceleration experiments (see for example Refs. 24 and 25).

The spectral analysis of proton beam gives us fundamental information: (i) the integrated (over a RCFs surface) energy spectrum (Fig. 9) and (ii) the divergence as a function of energy (the angular divergence can be calculated starting from the diameter of the spatial profiles functions for each discrete energy and the proton source-detector distance). These results are implemented as initial condition for the MC simulations together with the density profiles obtained by CHIC code modified following the scheme showed in the previous section (plasma effects).

A quantitative analysis of the energy and spatial distributions of protons after they are passed through the cylinder has been done starting from RCF images obtained by shots with cylindrical target. The integrated energy spectrum of the proton beam after passing through the cylinder (see Fig. 9) shows a consistent reductions of number of particle in the low energy region ($E_p < 4$ MeV). This is due to the fact that proton with energy below that value of energy overcomes a maximum areal density of the order of 13 mg/cc which is the typical mean value of the dense plasma core in our conditions.

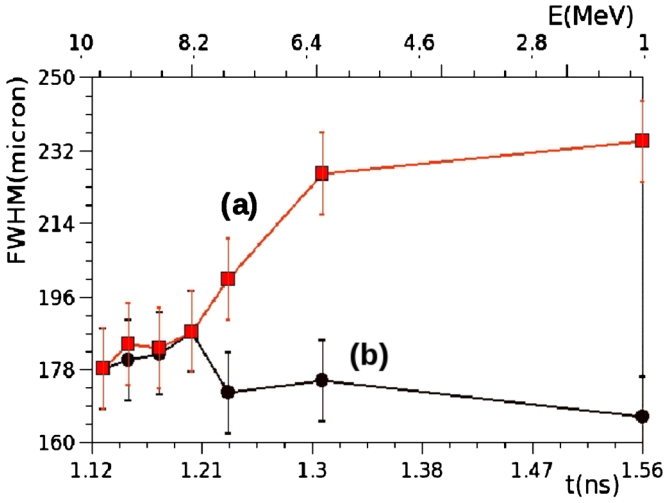

FIG. 12. (Color online) Comparison between FHWM of compressed cylinder (shot 9) by MC simulations obtained by using images on layers due to the respective Bragg peak energy (a) or convolving all the proton energies contribution as a function of layers (time or energy) for each layer (b). In the (b) case, the contribution due to the more energetic protons reduce drastically the apparent size of image formed in the lower energies layers.

C. Simulations results

Simulations of image formations were finally done as follows: (i) We assume a time sampling of hydroprofiles (density, temperature, and ionization degree (Figs. 6 and 7). (ii) For each hydrotime, we run a MC simulation using the relative proton energy and protons number, calculating the energy deposition in each RCF layer. Each hydrotime corresponds to a different time-of-flight of incoming protons, i.e., to a different proton energy. [The total number of particle (normalized to 1) used in all simulations must be equal to 1]. However, here we consider the energy deposited by such protons *in all* RCF layers and not only in the one corresponding to the Bragg peak of the *emitted* protons, as it is usually done (of course, images will be formed only in RCF layers before that corresponding to the *initial* Bragg peak and in this one). (iii) The full proton spectrum is covered running different simulations changing hydrotimes (i.e., the hydroprofiles).

In this way, for each RCF layer we get a series of monoenergetic, fixed-time, 2D images. (iv) Finally for each RCF layer, we sum all images at different times. In this way the resulting images on each layer will contain the contribution of all the protons of the beam, which probed the target at different times (depending on their energy).

The effects of image mixing is shown for instance in Fig. 12. Single energy images (obtained by considering Bragg peak deposition only) show a trend to increase target size as implosion proceeds, in disagreement with hydrosimulation results. Multienergy mixed images show instead the opposite trend. This is due to the fact that the convolution of the

synthetic images depends on the proton beam spectrum after passing through the compressed target which shows a consistent reduction in the low energy region.

These synthetic images (Fig. 13) can be compared to experimental ones (Fig. 5). Let us notice that in our energy ranges, as specified below, the protons directly traveling through the central axis of the compressed cylinder will suffer severe energy losses and severe MS. Therefore they will either not emerge from the cylinder, or emerge with a much reduced energy (therefore depositing their dose in another RCF layer), or finally, emerge with large scattering angles, so that they will be diffused over the entire layer surface. Therefore, the image formation will rather be done in *negative* by protons traveling around the central part of the compressed cylinder.

Following the analysis procedure which we applied to experimental data, we have extracted FWHM by using Gaussian and super-Gaussian fits (Fig. 14). We find, in agreement with experimental observations, a transition from super-Gaussian profiles at early times to Gaussian ones later in time. (Let us notice that in our synthetic images the compression is 2D, i.e., it is uniform in the direction of the cylinder axis. What we see at the edges of the compressed cylinder is simply due to modulation of MS effects). The full compression time is covered considering three different shots: shot $n°9$ from 1.1 to 1.5 ns $E_{\max} \sim 10$ MeV, shot $n°5$ from 1.5 to 1.9 ns $E_{\max} \sim 10$ MeV and shot $n°3$ from 2.0 to 2.4 ns $E_{\max} \sim 6$ MeV.

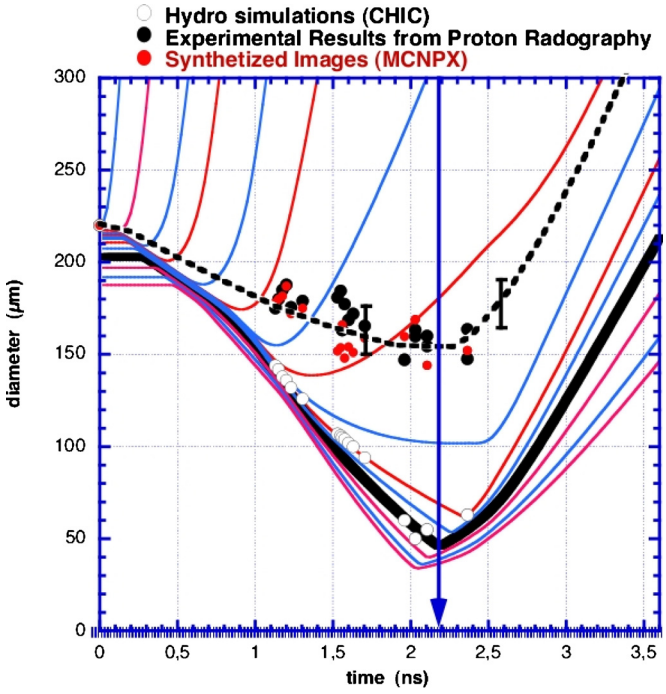

FIG. 14. (Color online) Comparison of experimental and simulation results. The point at 220 μm shows the initial diameter of the cylinder; empty circles show simulated results obtained running hydro code CHIC, full ones the experimental points (dark in print) and the simulated results running MCNPX MC code using hydro density profiles as input.

V. PHYSICAL INTERPRETATION

The apparent difference between proton radiography experimental and MC simulations results compared to the hydrodynamical expectation value and x-ray radiography results should be investigated more deeply in order to understand the physical meaning of this fact. In particular the relevant difference between proton (charge particle) and x-ray (neutral particle) is given by the fact that protons interact with the Coulomb field of the nuclei that are within the probed matter. The number of those interaction is huge (i.e., MS) and must be evaluated using statistical methods. In the following we investigate the MS phenomena and its influence in PR resolution.

A. Multiple scattering effects

It is important to perform an analytical evaluation of MS because it is really the main responsible of the observed larger size of the proton images. This allows to evaluate the right object size and also (as we will do in the last part of this paper) to evaluate the necessary conditions for getting good proton radiographies.

We can estimate the effect of MS on the *detected* size of the cylinder, by defining the blurring factor as

$$\xi = L\vartheta; \quad \vartheta = \frac{E_s}{2}\sqrt{\frac{1}{L_R}}\frac{\sqrt{A[\mathrm{g/cm^2}]}}{E[\mathrm{MeV}]}; \quad A = \int_{-\infty}^{\infty} \rho(x)dx, \quad (7)$$

where A is a generalization of the areal density for cylindrical geometry (usually A is defined as the product of the density times the longitudinal extension of the probed material), L is the distance between the cylinder and detector, θ is the mean angular deflection of a proton with energy E_p traversing a material with density ρ, E_s is a constant=15 MeV, and L_r is the radiation length,

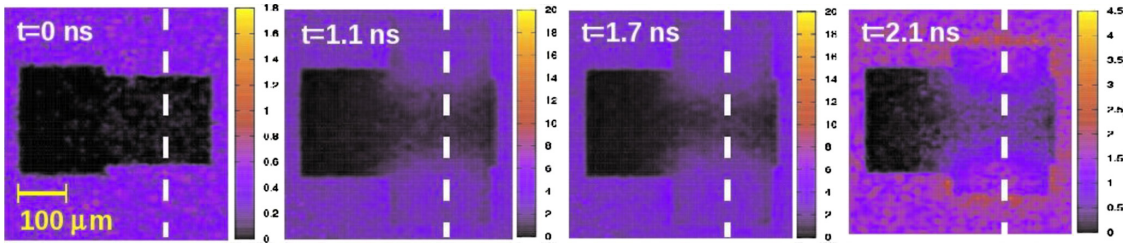

FIG. 13. (Color online) Compression history obtained by simulated proton radiographs at times $t_1=0$ ns, $t_2=1.1$ ns, $t_3=1.7$ ns, and $t_4=2.1$ ns.

$$\frac{1}{L_R[\mathrm{g/cm^2}]} = 1.4 \times 10^{-3} \frac{Z^2}{A} \ln\left(\frac{181}{\sqrt{Z}}\right). \quad (8)$$

Equation (7) was obtained by Rossi in Ref. 19 using a definition for the radiation length which is different from the one used today[26] so when using this formula, one must be careful to take this difference into account.

At each hydro time, the approximate size D_i of the image formed on the kth layer will be convolution of the *real size* ϕ_ι of the cylinder image with the blurring coefficient ξ_ι,

$$D_i = \frac{1}{M}\sqrt{(\phi_i M)^2 + \xi_i^2}. \quad (9)$$

Finally, the image formed on the layer k will have a size D_k given by the FWHM of the image $I_k = \Sigma_\iota I_{i,k}$ obtained by the convolution of all the images $I_{k,i}$.

In principle, Eq. (9) can be inverted deducing the *real size* of the cylinder for each layer. In order to estimate MS effect using the Rossi formula in Eq. (7) we should calculated the areal density A [Eq. (7)]. The areal density is usually defined in planar target geometry as the product between the density of the material (which is assumed constant) and the thickness of the target (along the direction perpendicular to the target surface). If the density profile along the longitudinal direction is not constant, this agrees with the so-called Gaussian approximation (the product of the peak density with the FWHM). In this experiment (and generally in all ICF experiments) the cylinder density profile cannot be represented by a Gaussian function (see Fig. 6) it is instead characterized by three regions: (i) the plasma corona (low density but large size), (ii) the shocked region (high density short distance), and (iii) the unperturbed target (original target density). Hence the proton traveling inside the target will see the value of the peak density only for short distance (~ 20 μm). In these conditions the Gaussian approximation leads to an overestimation of the blurring coefficient and the areal density must be calculated by detailed integration of the density profiles [Eq. (7)]. Moreover in this experiment the produced protons had a relatively low energy, the energy loss when they cross the target, and the MS effects are therefore quite large. In particular the protons passing through the dense core of the imploded target are scattered more than the protons passing through the external plasma corona so the images on layers are mainly formed in *negative* by *external* protons. In this case the areal density in Rossi's formula must be calculated by integrating the density profile only in the plasma corona region (i.e., considering external protons only).

Figure 15 shows estimations of the cylinder size (FWHM) for shot $n°9$ using Rossi's formula to calculate blurring coefficient and assuming different definition of the areal density A. The estimation based on the Gaussian approximation is far from simulation predictions while the estimations based on numerical integration of the hydrodensity profile are more precise. It is important to note that, as we have mentioned before, for low energy (first layers) A must be calculated only in plasma corona region.

The paper reported in Ref. 4 modeled the propagation of protons through the target using an algorithm based on the

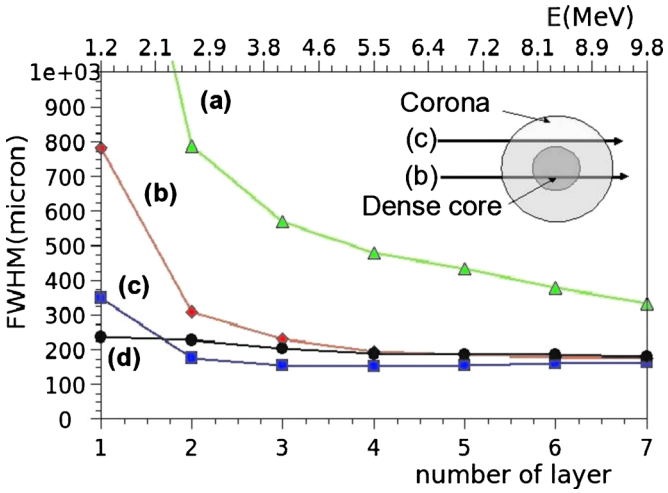

FIG. 15. (Color online) Estimation of cylinder size as a function of different layers (monoenergetic images for shot $n°9$) using Rossi's formula [Eq. (7)] and assuming different definition of the areal density: (a) Gaussian approximation $A = \rho L$, (b) numerical integration of density profile for protons traveling into the center of the compressed cylinder $A[-r_c, r_c]$ (where r_c is the core radius), (c) numerical integration of density profile over all space $A[-\infty, \infty]$, and (d) numerical integration of density profile in plasma corona region only $A[-\infty, r_c \cup r_c, \infty]$.

SRIM code,[10] which is in principle quite similar to MCPNX. However, the authors did not take into account the plasma effects and, as we already said, they only analyzed a single experimental image at fixed time neglecting the whole time evolution of the imploding target and the contributions from protons of different energies, i.e., they neglected *image mixing*. In this way they oversimplified the physical interpretation of the experimental results. Furthermore they estimated MS effects in a wrong way, by calculating the blurring coefficient [Eq. (7)] using density of the order of that of the compressed core [Fig. 15(b)], instead of the low density region [Fig. 15(c) or Fig. 15(d)], which is typical of the plasma corona. The resulting blurring coefficient increases and the resulting size prediction is $I \sim 160$ μm, which is far from the experimental results $I \sim 120$ μm. Finally the authors were unable to justify the large target size observed in proton radiography images, and in order to explain the difference they claimed for additional *exotic* effects due to electric fields in the target. We have show in this paper that there is no need for such additional effect and that, if properly taken into account, the hydrodynamics alone can completely justify the observed images.

B. Proton radiography oesolution

In this paper we have shown that the mechanism of PR in warm dense matter (ICF experiment) is quite different from that in cold matter due to the presence of a large number of collisions. Many MC simulations were made[4] but were never introduced any criterion for measuring the resolution of proton radiography in ICF.

Here we want to define a criterion to estimate the resolution degree of the system starting from the parameters and the experimental setup. To do this let us consider the experimental setup shown in Fig. 16(a) in which a pointlike proton

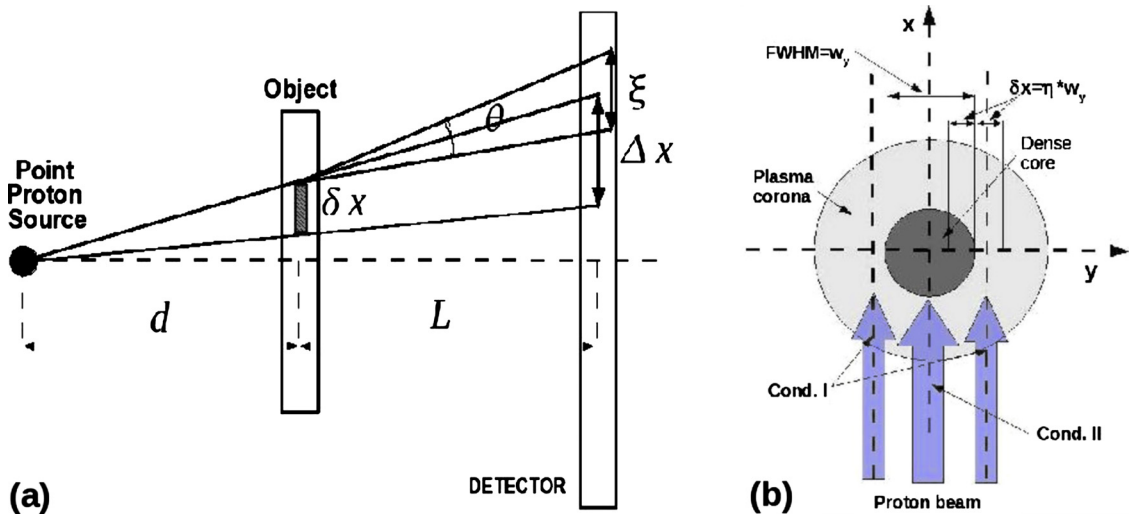

FIG. 16. (Color online) (a) Scheme of proton radiography resolution. (b) Scheme of "weak condition".

source irradiates a finite size object projecting its image on the detector. In principle, if the MS is negligible, the object will appear transparent (i.e., $\rho=0$) and the projected image size will appear enlarged by a factor M [Eq. (9)] which corresponds to the geometrical magnification.

More specifically, defining a generic distance between two points in the object δx, the projected size on the detector becomes $\Delta x=M\ \delta x$. Nevertheless the effect of the Coulomb MS is never negligible and the protons passing through the object are deflect by a mean angle q giving a mean displacement $\xi=L\theta$ which can be estimate using the Rossi's formula in Eq. (7).

Therefore the projected image on the detector will appear enlarged by a factor μ with respect to that would appear if there were no scattering Δx, i.e., by a factor μM with respect to the initial distance δx [we start from Eq. (9) using Δx instead of f],

$$\mu=\sqrt{1+\left(\frac{\bar{\xi}}{\delta x}\right)^2};\quad \bar{\xi}=\xi/M. \tag{10}$$

Starting from the above considerations, we can infer that the blurring coefficient must remain less or of the same order than resolution that we would like to obtain dx in order to avoid the crossover between different single proton trajectory and the consequent loss of the initial spatial target information's carry on by protons.

The above-mentioned condition can be written in terms of blurring coefficient (i.e., ξ/M is the resolution of our system in analogy with Rayleigh's criterion in optics)

$$0\le\bar{\xi}\le\delta x \tag{11}$$

or in terms of the a-dimensional parameter m

$$1\le\mu\le\sqrt{2}. \tag{12}$$

We refer to the above condition [Eqs. (11) and (12)] as the "strong condition." If the strong condition is satisfied we can use proton radiography in conventional way and the gray scale obtained by the RCF analysis will be proportional to the density gradient of the probed target.

A simple estimation of the μ parameter can be done starting from the protons passing through the dense core in our case: the size of the core is $\sim$60 mm then we look for a resolution $\delta x\sim 20$ μm; the blurring coefficient ξ/M can be estimated assuming the maximum energy for protons (10 MeV), which are passing through an area density $A\sim 0.05$ g/cm^2 and a magnification factor $M=4.5$. The result is $\mu\sim 7$ which is larger than the maximum permitted value in Eq. (12) confirming that for low energy protons the strong condition cannot be applied because of they are not able to probe the dense core. On the other hand, assuming the plasma corona areal density $A\sim 0.002$ g/cm^2 at the same conditions we obtain $\mu\sim 2$ which is a more reasonable value.

In Fig. 17 is shown the mean scattering angle versus areal density for different proton energy. Typical value for our experiment is shown. The maximum resolution obtained in the region of the plasma corona at the RAL-08 experiment is about 20 μm due to the low energy of the probed protons ($<$10 MeV), while if we would like to probe a typical core density target in omega[27] we need to use a very high energy proton beam ($\sim$250 MeV).

The grey region corresponds to the ST limit obtained by fitting simulations based on the ions ST formula in Eq. (1). In particular we calculated the minimum energy required for a proton to overcome certain areal density of carbon ($Z=6$ A=12) $E_m[\mathrm{MeV}]\approx 30\sqrt{A[\mathrm{g/cm^2}]}$. Inserting the minimum energy into the Rossi formula for the mean scattering angle [Eq. (7)] we obtain the maximum scattering angle for proton to overcome certain areal density $\vartheta_m\approx\sqrt{A[\mathrm{g/cm^2}]}/E_m[\mathrm{MeV}]\approx 1.9°$ (i.e., protons with scattering angles lower than the maximum will overcome the areal density).

The above considerations suggest that proton radiogra-

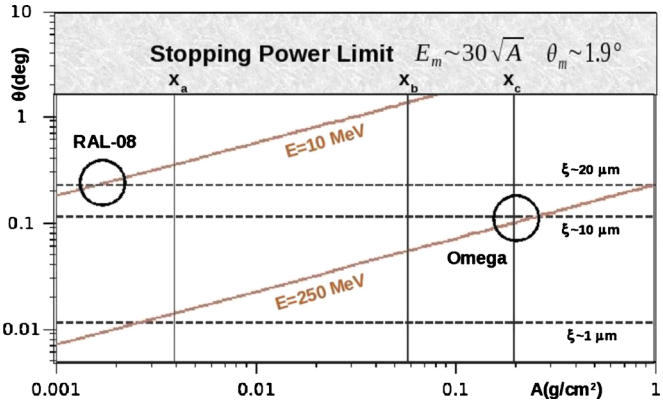

FIG. 17. (Color online) Mean scattering angle q vs areal density for different proton energies. x_a $A \sim 0.004$ g/cm^2 proton trajectory calculated through plasma corona and x_b $A \sim 0.05$ g/cm^2 trajectory through core for the present experiment, and x_c $A \sim 0.2$ g/cm^2 trajectory (theory) for a typical omega target (Ref. 27). If we assume $d=L=1$ cm ($M=2$) we get the corresponding spatial resolution limits: ~20 μm, ~10 μm, or ~1 μm (horizontal dashed lines). The grey region corresponds to the ST limit $\theta_{\max} \sim 1.9°$. The intersection between red (lighter) and dashed lines represent the resolution reachable at that energy and a real density value.

phy technique can be used for ICF only under specific conditions which depend also on the geometrical features of the experiment.

As example let us assume very sharp target density profiles; as just explained before, protons which pass through the dense core are stopped or diffuse while those which pass through the corona are deviated by a mean scattering angle which could be acceptable. Thanks to the sharp profiles, the differences in areal density between the external and the internal protons become be very huge giving a high contrast and then an acceptable resolution.

Here we developed a criterion to estimate the resolution of the system in the above mentioned condition as a function of the sharpness of the target profile and we refer to this criterion as "weak condition."

Let start assuming a 2D super-Gaussian density profile (where g is related to slope of the distribution)

$$A_{x,y}(\gamma) = \rho_p \exp\left[-\ln 2\left(\frac{x^\gamma + y^\gamma}{w^\gamma}\right)\right] \tag{13}$$

(where we have defined w=FWHM/2). Protons arriving by the x-direction will probe certain density profiles $A_y(g)$ as a function of their y position

$$A_y(\gamma) = \int_R A_{x,y}(\gamma)dx = A_x(\gamma)\exp\left[-\ln 2\left(\frac{x}{w}\right)^\gamma\right];$$
$$A_x(\gamma) = \rho_p \int_R \exp\left[-\ln 2\left(\frac{x}{w}\right)^\gamma\right]dx. \tag{14}$$

The resulting Blurring coefficient will be

$$\xi_y(\gamma) = \frac{\Gamma c\sqrt{A_y(\gamma)}}{E_p} = \frac{\Gamma c\sqrt{A_x(\gamma)}}{E_p}\exp\left[-\frac{\ln 2}{2}\left(\frac{x}{w}\right)^\gamma\right]; \tag{15}$$

$$\Gamma = \frac{L}{M} = \frac{Ld}{L+d};\quad c = \frac{E_s}{2\sqrt{L_R}}.$$

Following the scheme in Fig. 16(b), the weak condition can be written as follows:

(i) The blurring occurring by protons passing through the plasma corona (region of the density distribution outside the FWHM) must be of the same order of the resolution ($\delta x = 2hw$) which we would like to obtain (the resolution must be a fraction of the FWHM).

(ii) The blurring occurring by protons passing through the plasma core (region of the density distribution inside the FWHM) must be larger than the two FWHMs of the target density profiles,

$$(I)\xi_{(w+2\eta w)}(\gamma) < 2\eta w;\quad (II)\xi_{(w-2\eta w)}(\gamma) > 4w.$$

The above conditions can be rewritten as follows:

$$(I)2^{(1/2)[1+2\eta]^\gamma} - \frac{\Gamma c\sqrt{A_x\rho_p}}{2\eta w E_p} > 0;$$

$$(II)\frac{\ln 2}{2}[(1+2\eta)^\gamma - (1-2\eta)^\gamma] + \ln\left(\frac{\eta}{2}\right) > 0.$$

The (i) condition depends on the experimental parameters (ρ, E_p, w, Γ) and on the geometry of the target density profiles (γ, η) it gives us the resolution of proton radiography for all the protons passing outside of the core which is defined by the FWHM. The (ii) condition depends on the geometry of the target density profiles (γ, η) and it guarantees that the protons passing through the core do not participate to form the image on layer.

Of course in the weak condition regime we accept to loss all the information about the internal core of the target and we look at its size only.

From experimental point of view the super-Gaussian degree g is not convenient in anyway we can use the relation between the Gaussian degree g and the slope of the density profiles calculated in w [$A'(w)$]

$$A'(w) = \frac{\ln 2}{2}\left(\frac{\rho_p}{w}\right)\gamma. \tag{16}$$

Let us check the weak condition for the two interesting cases: RAL-08 (Refs. 10 and 11) and omega typical experiments.[25] The (ii) condition is independent on the experimental parameters and it leads to the conditions: $\delta x > 20$ μm for $\gamma=2$ and $\delta x > 10$ μm for $\gamma=4$. The (i)_ condition gives $\delta x > 85$ μm for $\gamma=2$, $\delta x > 30$ μm for $\gamma=4$, and $\delta x > 15$ μm for $\gamma=6$ for the RAL-08 experiment ($\rho \sim 5$ g/cc, $E \sim 10$ MeV, $w \sim 60$ μm), and gives $\delta x > 90$ μm for $\gamma=2$, $\delta x > 30$ μm for $\gamma=4$, and $\delta x > 18$ μm for $\gamma=6$ for a typical omega target ($A \sim 0.2$, $E \sim 15$ MeV, $w \sim 60$ μm).

VI. CONCLUSIONS

PR has been used to diagnose the implosion of cylindrical targets, but a detailed analysis is required in order to allow comparison with hydrosimulations. The simple RCF-

layer-to-time relation does not hold here because of *image mixing*. The information carried on by protons passing through the dense core is lost because they are scattered more than the protons passing through plasma corona. The last ones then form the images on detectors "*in negative*." Moreover, we have shown that in conditions in which the experiment has been performed, ST is higher in low density plasma than in cold matter and how we can take into account this effect in MC simulation. In any case, even if the time history and stagnation time are reproduced correctly, low-energy protons are not able to probe the dense core directly. MS is reduced for high-energy protons and, with respect to this problem, we have deduced two different criteria to predict the minimum energy needed in order to reach a good resolution in ICF experiments.

ACKNOWLEDGMENTS

The authors acknowledge the support of the HiPER project and Preparatory Phase Funding Agencies (EC, MSMT, and STFC) in undertaking this work.

APPENDIX: PROTON ST

For our intent we prefer to write all the formulas in unit of MeV for proton beam energy E_p, g/cc for density ρ of the probed material, and eV for the temperature k_bT of the plasma. We start writing the classical nonrelativistic Bethe SP formula for cold matter,[17]

$$\left(\frac{dE}{dx}\right)_c = 1.23 \times 10^{23}\frac{\rho Z}{AE_p}L_b, \tag{A1}$$

where

$$\ln\left(2149\frac{E_p}{\bar{I}}\right); \quad \bar{I} = 8Z\left(1+\frac{1.8}{\sqrt{Z}}\right). \tag{A2}$$

Equation (A1) represents the energy loss by proton with energy E_p passing through a material with atomic and mass numbers Z and A and solid density $\rho_c=(A/Z)(n_b/N_a)$ where n_b is the bound electrons density, and N_a the Avogadro number and is the mean ionization potential. When the proton beam passes through a plasma instead of cold matter, Eq. (A1) is not able to describe all the physical phenomena occurring during the interaction as for example the temperature effects. The right SP formula can be obtained starting from a self-contained representation of the theory of energy loss of ions penetrating classical plasma given by nonrelativistic Vlasov–Poisson equations,[19]

$$\left[\partial_t + \vec{v}\cdot\partial_{\vec{r}} + \frac{e}{m}(\partial_{\vec{r}}\phi)\cdot\partial_{\vec{v}}\right]f(\vec{r},\vec{v},t) = 0; \tag{A3}$$

$$\nabla^2\phi = -4\pi Ze\,\delta(\vec{r}-\vec{v}t) + 4\pi e\int f(\vec{r},\vec{v},t)d^3v - 4\pi n_0 e$$

which leads to the following solution:

$$\left(\frac{dE}{dx}\right)_p = 1.23 \times 10^{-9}\frac{\rho}{AE_p}[q_iL_f + (Z-q_i)L_b], \tag{A4}$$

where

$$L_f = G(x)\ln(\lambda_d k) + H(x)\ln(x), \tag{A5}$$

$$G(x) = erf\left(\frac{x}{\sqrt{2}}\right) - \sqrt{\frac{2}{\pi}}x\exp(-x^2/2), \tag{A6}$$

$$H(x) = \frac{x^3}{3\sqrt{2}\pi\ln(x)}\exp(-x^2/2) + \frac{x^4}{x^4+12}, \tag{A7}$$

$$x = 33\sqrt{\frac{E_p}{K_bT}}; \ (A8); \ \lambda_d = 7.6\times10^{-12}\sqrt{\frac{AK_bTE_p}{q_i\rho_p}}, \tag{A8}$$

$$k = Min[7.46\times10^{11}(E_p + 1.8\times10^{-3}K_bT), 2.4\times10^{11}\sqrt{E_p}]. \tag{A9}$$

Here λ_d is the Debye length in unit of m, k in m^{-1} is the inverse of the impact parameter, and $\rho_p=(A/q_i)(n_f/N_a)$ is the plasma density with n_f defined as the free electron density. The above equations can be derived assuming two conditions which must be always satisfied:[19] (c1) Free gas Maxwell–Boltzmann statistic approximation and (c2) collisionless approximation.

With our notation the above conditions can be written as

$$K_bT[\text{eV}] > 66.7\left(\frac{q_i}{A}\right)^{2/3}\rho^{2/3}[\text{g/cc}] \approx K_bT > 42\rho^{2/3}, \tag{A10}$$

$$K_bT[\text{eV}] > 58.8\left(\frac{q_i}{A}\right)^{1/3}\rho^{1/3}[\text{g/cc}] \approx K_bT > 46.7\rho^{1/3}. \tag{A11}$$

Assuming a completely ionized ($q_i=6$) carbon target ($A=12$) we obtain:

Figure 18 shows the region of temperature-density plane [completely ionized ($q_i=6$) carbon target ($A=12$)] in which conditions c1 and c2 are satisfied. The filled circles represent the three different state of the target in RAL-08 experiment. Note that SP formula in Eq. (A5) is able to describe the energy loss by protons in the plasma corona region only and partially in the plasma core region (high density and temperature). The cold region can be described also by Eq. (A5) in the limit of nonionized plasma ($q_i=0$, i.e., solid state) in which it becomes equal to Eq. (A4). For ICF physics, the temperature of the proton beam which probed the target ($\sim$10 MeV) is always greater than the temperature of the probed plasma ($\sim$1 KeV), then the free term in Eq. (A5) becomes

$$(A5_{bis})L_f \approx \ln\left(60\sqrt{\frac{AE_p^2}{q_i\rho_p}}\right) \tag{A12}$$

which leads to the following simplified formula [starting from Eq. (A4)]:

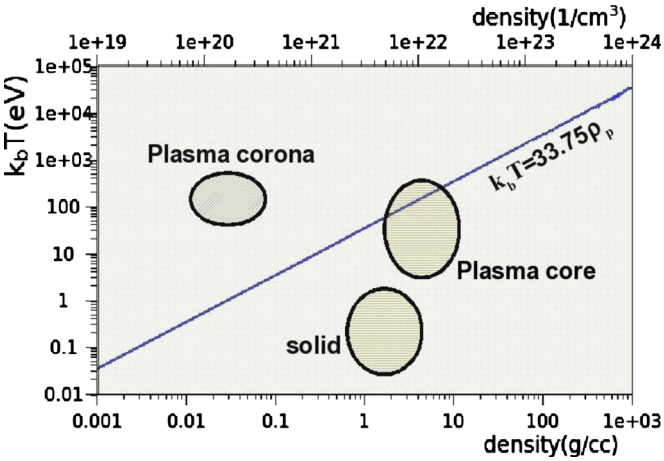

FIG. 18. (Color online) Temperature (eV) vs density (g/cc) plane. The filled circle regions represented by the graph represent the three different states of matter occurring in RAL-09 experiment. The region above the blue (darker) line ($T>42\rho_p$) is that in which the conditions in Eq. (A11) is satisfied while the region above the red (lighter) line ($T>46.7\rho_p$) is that in which the conditions in Eq. (A11) are satisfied.

$$(A6_{bis})\left(\frac{dE}{dx}\right)_p = 1.23\times10^{-9}\frac{q_i\rho}{AE_p}\left[\ln\left(60\sqrt{\frac{AE_p^2}{q_i\rho_p}}\right) + \frac{(Z-q_i)}{q_i}\ln\left(2149\frac{E_p}{\bar{I}}\right)\right]. \quad \text{(A13)}$$

[1] *Advanced Diagnostics for Magnetic and Inertial Fusion*, edited by E. Stott, A. Wootton, G. Gorini, and D. Batani (Plenum, New York, 2002).
[2] J. R. Rygg, F. H. Séguin, C. K. Li, J. A. Frenje, M. J.-E. Manuel, R. D. Petrasso, R. Betti, J. A. Delettrez, O. V. Gotchev, J. P. Knauer, D. D. Meyerhofer, F. J. Marshall, C. Stoeckl, and W. Theobald, Science **319**, 1223 (2008).
[3] A. J. Mackinnon, P. K. Patel, M. Borghesi, R. C. Clarke, R. R. Freeman, H. Habara, S. P. Hatchett, D. Hey, D. G. Hicks, S. Kar, M. H. Key, J. A. King, K. Lancaster, D. Neely, A. Nikkro, P. A. Norreys, M. M. Notley, T. W. Phillips, L. Romagnani, R. A. Snavely, R. B. Stephens, and R. P. J. Town, Phys. Rev. Lett. **97**, 045001 (2006).
[4] M. Borghesi, A. Schiavi, D. H. Campbell, M. G. Haines, O. Willi, A. J. MacKinnon, L. A. Gizzi, M. Galimberti, R. J. Clarke, and H. Ruhl, Plasma Phys. Controlled Fusion **43**, A267 (2001).
[5] C. N. Danson, L. J. Barzanti, Z. Chang, A. E. Damerell, C. B. Edwards, S. Hancock, M. H. R. Hutchinson, M. H. Key, S. Luan, R. R. Mahadeo, I. P. Mercer, P. Norreys, D. A. Pepler, D. A. Rodkiss, I. N. Ross, M. A. Smith, R. A. Smith, P. Taday, W. T. Toner, K. W. M. Wigmore, T. B. Winstone, R. W. W. Wyatt, and F. Zhou, Opt. Commun. **103**, 392 (1993).
[6] M. Dunne, F. Amiranoff, S. Atzeni, J. Badziak, D. Batani, S. Borneis, J. L. Collier, C. N. Danson, J. C. Gauthier, J. J. Honrubia, M. H. R. Hutchinson, S. Jacquemot, M. Koenig, K. Krushelnick, T. Mendonca, P. V. Nickles, P. A. Norreys, S. J. Rose, J. Wolowsk, N. Woolsey, M. Zepf *et al.* "HiPER, technical background and conceptual design," Rutherford Appleton Laboratory Report No. RAL-TR-2007–008, 2007.
[7] F. Perez, M. Koenig, D. Batani, S. D. Baton, F. N. Beg, C. Benedetti, E. Brambrink, S. Chawla, F. Dorchies, C. Fourment, M. Galimberti, L. A. Gizzi, R. Heathcote, D. P. Higginson, S. Hulin, R. Jafer, P. Koester, L. Labate, K. Lancaster, A. J. MacKinnon, A. G. McPhee, W. Nazarov, P. Nicolai, J. Pasley, A. Ravasio, M. Richetta, J. J. Santos, A. Sgattoni, C. Spindloe, B. Vauzour, and L. Volpe, Plasma Phys. Controlled Fusion **51**, 124035 (2009).
[8] B. Vauzour, F. Perez, L. Volpe, K. Lancaster, Ph. Nicolaı, M. Koenig, D. Batani, S. D. Baton, F. N. Beg, C. Benedetti, E. Brambrink, S. Chawla, F. Dorchies, C. Fourment, M. Galimberti, L.A. Gizzi, R. Heathcote, D. P. Higginson, S. Hulin, R. Jafer, P. Koster, L. L. Labate, A. J. MacKinnon, A. G. MacPhee, W. Nazarov, J. Pasley, C. Regan, X. Ribeyre, M. Richetta, G. Schurtz, A. Sgattoni, and J. J. Santos, "Laser-driven cylindrical compression of target for fast electron transport study in warm and dense plasmas," Phys. Plasmas (submitted).
[9] R. Jafer, L. Volpe, D. Batani, M. Koenig, S. Baton, E. Brambrink, F. Perez, F. Dorchies, J. J. Santos, C. Fourment, S. Hulin, P. Nicolai, B. Vauzour, K. Lancaster, M. Galimberti, R. Heathcote, M. Tolley, Ch. Spindloel, P. Koester, L. Labate, L. Gizzi, C. Benedetti, A. Sgattoni, M. Richetta, J. Pasley, F. Beg, S. Chawla, D. Higginson, A. MacKinnon, A. McPhee, D.-H. Kwon, and Y. Rhee, J. Korean Phys. Soc. **57**, 305 (2010).
[10] M. L. Fensin, J. S. Hendricks, and S. Anghaie, J. Nucl. Sci. Technol. **170**, 68 (2010); F. Ziegler, J. P. Biersack, and M. D. Ziegler, *The Stopping Power of Ions in Matter* (Lulu Press, Morrisville, North Carolina, 2009).
[11] P. H. Maire, J. Breil, R. Abgral, and J. Ovadia, SIAM J. Sci. Comput. (USA) **29**, 1781 (2007).
[12] A. J. Kemp and J. Meyer-ter-Vehn, Nucl. Instrum. Methods Phys. Res. A **415**, 674 (1998)
[13] T4 Group, "SESAME Report on the Los Alamos Equation of State Library," Los Alamos National Laboratory, Los Alamos Report No. LALP-83-4.
[14] M. Borghesi, A. J. Mackinnon, D. H. Campbell, D. G. Hicks, S. Kar, P. K. Patel, D. Price, L. Romagnani, A. Schiavi, and O. Willi, Phys. Rev. Lett. **92**, 055003 (2004).
[15] D. Batani, S. D. Baton, M. Manclossi, D. Piazza, M. Koenig, A. Benuzzi-Mounaix, H. Popescu, C. Rousseaux, M. Borghesi, C. Cecchetti, and A. Schiavi, Phys. Plasmas **16**, 033104 (2009).
[16] M. Roth, A. Blazevic, M. Geissel, T. Schlegel, T. E. Cowan, M. Allen, J.-C. Gauthier, P. Audebert, J. Fuchs, J. Meyer-ter-Vehn, M. Hegelich, S. Karsch, and A. Pukhov, Phys. Rev. ST Accel. Beams **5**, 061301 (2002).
[17] See http://www.gafchromic.com/ for GAFCHROMIC HD-810 radiochromic dosimetry film and D-200 preformatted dosimeters for high-energy photons configurations.
[18] H. Bethe, Ann. Phys. (N.Y.) **5**, 325 (1930).
[19] B. Rossi and K. Greisen, Rev. Mod. Phys. **13**, 240 (1941).
[20] T. A. Mehlhorn, J. Appl. Phys. **52**, 6522 (1981).
[21] T. Peter and J. Meyer-ter-Vehn, Phys. Rev. A **43**, 1998 (1991); **43**, 2015 (1991).
[22] F. C. Young, D. Mosher, S. J. Stephanakis, S.A. Goldtein, and T. A. Mehlhorn., Phys. Rev. Lett. **49**, 549 (1982).
[23] N. Bohr, Philos. Mag. **30**, 581 (1915).
[24] E. Breschi, Nucl. Instrum. Methods Phys. Res. A **522**, 190 (2004).
[25] K. Zeil, S. D. Kraft, S. Bock, M. Bussmann, T. E. Cowan, T. Kluge, J. Metzkes, T. Richter, R. Sauerbrey, and U. Schramm, New J. Phys. **12**, 045015 (2010).
[26] See http://pdg.lbl.gov/2008/AtomicNuclearProperties for PDG particle data group.
[27] University of Rochester-Laboratory for Laser Energetics Report No. DOGNA28503-923, January 2010.